fluids

MDPI

Article

Instability and Transition of a Boundary Layer over a Backward-Facing Step

Ming Teng * and Ugo Piomelli

Department of Mechanical and Materials Engineering, Queen's University, Kingston, ON K7L 3N6, Canada; ugo@queensu.ca

* Correspondence: 17mt9@queensu.ca

Abstract: The development of secondary instabilities in a boundary layer over a backward-facing step is investigated numerically. Two step heights are considered, $h/\delta_o^* = 0.5$ and 1.0 (where δ_o^* is the displacement thickness at the step location), in addition to a reference flat-plate case. A case with a realistic freestream-velocity distribution is also examined. A controlled K-type transition is initiated using a narrow ribbon upstream of the step, which generates small and monochromatic perturbations by periodic blowing and suction. A well-resolved direct numerical simulation is performed. The step height and the imposed freestream-velocity distribution exert a significant influence on the transition process. The results for the $h/\delta_o^* = 1.0$ case exhibit a rapid transition primarily due to the Kelvin–Helmholtz instability downstream of step; non-linear interactions already occur within the recirculation region, and the initial symmetry and periodicity of the flow are lost by the middle stage of transition. In contrast, case $h/\delta_o^* = 0.5$ presents a transition road map in which transition occurs far downstream of the step, and the flow remains spatially symmetric and temporally periodic until the late stage of transition. A realistic freestream-velocity distribution (which induces an adverse pressure gradient) advances the onset of transition to turbulence, but does not fundamentally modify the flow features observed in the zero-pressure gradient case. Considering the budgets of the perturbation kinetic energy, both the step and the induced pressure-gradient increase, rather than modify, the energy transfer.

Keywords: DNS; transition; secondary instability; surface imperfection; backward-facing step

Citation: Teng, M.; Piomelli, U. Instability and Transition of a Boundary Layer over a Backward-Facing Step. *Fluids* **2022**, *7*, 35. https://doi.org/10.3390/fluids7010035

Academic Editor: Ramesh Agarwal

Received: 24 December 2021
Accepted: 12 January 2022
Published: 14 January 2022

1. Introduction

Laminar-turbulent transition is a complex, multi-stage process, through which a laminar flow becomes turbulent. The specific type of flow and the nature of the perturbation determines the type of transition, and its associated physical mechanisms [1]. Transition in boundary-layer flows can be categorized into two main classes, depending on the way it is induced. The first of them usually occurs when environmental perturbations are small ($O(10^{-4})$ of the freestream velocity, U_∞); this category typically includes the so-called H- and K-type transition. It is usually associated with the formation and amplification of Tollmien–Schlichting (T–S) waves, and involves the interaction of various instability modes that eventually lead to breakdown of the laminar flow. The various stages of the transition happen consecutively, up to the onset of turbulence. The second type is associated with direct breakdown of the laminar flow, and normally arises when high levels of perturbations ($O(10^{-2})$ of U_∞) are present; common sources of such perturbations include surface roughness or freestream turbulence. The evolution of this type of transition typically involves rapid and transient amplification of perturbations and bypasses the slowly growing phases of T-S waves, and is known as bypass transition [1,2].

One important source of perturbation that can induce transition (following either of the paths mentioned before) are the surface imperfections that are inevitable in flows in engineering and the natural sciences. They may be due to the manufacturing process itself, to damage to the surface (pitting, cavitation, ice accumulation ...) or to the geometry itself

(terrain topology, vegetation). These imperfections may significantly affect the transition process, and are the subject of this work. Another factor that may play a role is the freestream pressure gradient, which occur, for example, over aircraft wings and engine nacelles. An adverse pressure gradient is known to amplify the transition process, and the combined effect of pressure gradient and surface imperfections may alter the transition process very considerably. The combined effect of surface imperfections and freestream pressure-gradients is the subject of this study. In the remainder of this Section the studies of the effects of imperfections and adverse pressure-gradients are reviewed separately. The objectives of this work will then be outlined.

1.1. Influence of Localized Surface Imperfections

Surface imperfections can be categorized based on their geometry. They can be two-dimensional (such as forward- or backward-facing steps, cylinders, gaps and surface waviness) or three-dimensional (for instance, spheres, cubes, or roughness elements, etc.) [3–6]. Surface imperfections give rise to instability by one or more physical mechanisms, and those associated with laminar separation [4,7–11] and crossflow vorticity [6,12–14] have attracted much attention [3,15,16].

Dovgal & Kozlov [8] experimentally investigated the receptivity of the separation region induced in the boundary layer by two-dimensional (2D) roughness; among the geometries studied were square bumps, forward- and backward-facing steps (FFSs and BFSs, respectively). They observed that, for the step sizes examined ($h/\delta_{99} = 0.16$ and 0.38, where h and δ_{99} represent the step height and undisturbed boundary-layer thickness), the flow over a BFS was more destabilized compared to that over an FFS. Dovgal et al. [9] investigated this behavior theoretically using the Orr-Sommerfeld equation with a hyperbolic-tangent mean-velocity profile. They showed that the growth-rate of the perturbation and the range of unstable frequencies increased rapidly with the distance from the wall of the inflection point.

Boiko et al. [17] studied experimentally the flow instability of a laminar separation zone developed downstream of a roughness element; the element was rectangular in shape and $h/\delta_{99} = 0.35$. They observed that the frequencies and growth-rates of the propagating perturbations are similar to those of inviscidly unstable free-shear flows. More specifically, the perturbations within a recirculation zone seemed to rely mostly on the instability of the mixing layer at its edge; this conjecture was consistent with result of the numerical study by Nayfeh et al. [4] and Danabasoglu et al. [18].

An experiment by Wang [19] considered both steps and square bumps. The experiment revealed that the mean flow was more severely distorted downstream than upstream of the bump; the distortion range downstream of the bump was also larger in size. This led to a higher amplification of instability waves in the downstream region. The flow field upstream of the FFS and downstream of the BFS, in fact, is similar to than that in the region upstream and downstream of the bump, which explained the difference in the sensitivity to perturbations between forward- and backward-facing step. Wang & Gaster [20] investigated the effects of the step on the boundary-layer transition more in detail. A correlation between the transition Reynolds number (Re) and the relative step height was proposed for both backward- and forward-facing steps. The authors also confirmed that the BFS induced transition earlier than the FFS.

Duncan [21] studied the effect of steps on the boundary-layer transition on a swept wing; both forward- and backward-facing steps were considered in wind tunnel and flight test. It was conjectured that in both cases there is a critical step height, which depends on the Re. Below it, the crossflow instability is dominant, while once above the threshold, the Kelvin–Helmholtz (K–H) instability becomes primary. The critical height of the FFS could be twice that of a BFS: up to $h_{crit}/\delta^* \sim 1.5$ for FFS, and $h_{crit}/\delta^* \sim 0.6$ for BFS (h_{crit} and δ^* denote the critical step height and the local undisturbed displacement thickness). A recent work of Eppink et al. [14] studied the effects of a BFS on the transition of a crossflow-dominated boundary layer; the experiment considered three step heights on a swept flat plate, $h/\delta_{99} = 0.36$, 0.45, and 0.49, respectively. The significant influence of h/δ_{99}

on the amplitude of unsteady perturbation was observed, whereas the influence over the stationary crossflow vortex was limited. It was conjectured that the unsteady perturbation was the determining factor in transition. The accelerated onset of transition due to the step height was related to the change in transition mechanism, but this did not necessarily bypass the slowly growing phases of primary perturbations. Eppink [22] experimentally explored the effects of step shapes on transitional flow over a swept BFS ($h/\delta_{99} = 0.76$); the shape was modified by placing different ramps on the downstream face of the step. The experiment demonstrated the effectiveness of a 5% ramp in delaying the transition downstream of the step.

Hu et al. [23] investigated the supersonic transitional flow ($Ma_\infty = 1.7$) over a BFS using large eddy simulation. A fixed step height, $h = 3\delta_o$ (δ_o denotes the inflow boundary-layer thickness), was used; no perturbation was introduced. Five distinct stages were identified for the transition process downstream of the step where K-H, and then secondary instability dominated. Hu et al. [24] incorporated perturbations in the domain considered previously with two amplitudes introduced at the inflow boundary, $A/U_\infty = 0.1\%$ and 1.0%, respectively. The first case was analyzed in detail and revealed the dominant roles played by T-S and K-H modes simultaneously immediately downstream of the step. They conjectured that the K-H instability essentially served as an amplifier when primary T-S mode interacted with K-H mode initially; this amplification was consistent with observation in an earlier experiment by Eppink et al. [13] on the interaction of crossflow instability with a BFS ($h/\delta_{99} = 0.50$). The vortex breakdown was observed to take place close to the location of maximum enstrophy.

1.2. Influence of the Pressure Gradient

The freestream pressure-gradient plays an important role in boundary-layer transition, as demonstrated in the early experiment by Schubauer & Skramstad [25]; the favorable and adverse pressure-gradients (FPG/APG) respectively stabilized or destabilized initially small perturbations. Flows with APGs often have inflectional velocity profiles and, therefore, are subject to both viscous and inviscid K-H instability. Wazzan et al. [26] investigated the spatial stability of the Falkner–Skan similarity profiles systematically by solving the Orr-Sommerfeld equations; the Hartree parameter $\beta_H = 2m/(m+1)$ ranged from -0.1988 to 1.0; m is a dimensionless constant that determines the freestream-velocity profile (see below). The results showed that the increased growth-rates of the perturbations were related to the increases in the strength of the APG. Taghavi & Wazzan [27] focused on the Falkner–Skan profiles that gave rise to the reverse flows. The results, however, showed that the profile became more stable as β_H decreased from -0.05 to -0.18. The authors conjectured that this was due to the inflection-point locations in the wall-normal direction; the profile with $\beta_H = -0.05$ showed an inflection point 35% farther away from the wall, compared to that with $\beta_H = -0.18$.

Gostelow & Blunden [28] studied boundary-layer transition experimentally with both zero pressure gradient (ZPG) and a range of APGs. They considered the intermittency distribution, i.e., the percentage of time the boundary layer is turbulent. The transition lengths for APGs were shown to be much shorter than that for the ZPG case and self-similarity in intermittency distributions was observed. A later experimental work by Walker & Gostelow [29] studied the effect of an APG on the nature and length of a transitional boundary layer, and proposed a predictive correlation for transition that incorporated both *Re* and pressure-gradient effects.

Kloker & Fasel [30] carried out a direct numerical simulation (DNS) of transition in a decelerating boundary layer with a strong pressure gradient ($\beta_H = -0.18$). A narrow ribbon created small-amplitude, periodic perturbations leading to K-type transition. Compared to a Blasius case, the transitional flow underwent a rapid breakdown process, more complex in structure. The author examined the root-mean-square (*rms*) amplitude of the streamwise perturbation component, u'_{rms}, at different spanwise locations. At the late stages, the disturbance grew faster in regions where u'_{rms} was minimal ("valleys") than in the regions where it was high ("peaks").

Experiments by Mislevy & Wang [31] measured mean quantities in transitional, thermal and momentum boundary layers. Borodulin et al. [32] experimentally investigated the production mechanism at the late non-linear stages of transition in a self-similar APG boundary layer ($\beta_H = -0.115$); a 2D harmonic T-S wave (4% of local U_∞), initially perturbed by weak broadband disturbances, was introduced to initiate the transition. Formation and evolution of flow structures were qualitatively similar to those seen in a similar ZPG case. The authors conjectured that there exist a universal, essentially non-linear, mechanism for the turbulence production in wall-bounded shear flows.

In a recent DNS study, Bose et al. [33] examined the bypass transition in an APG boundary layer with $\beta_H = -0.14$. Effects of the inflow freestream-turbulence (FST) intensity and the disturbance spectrum on the transition were considered. At low FST intensity (0.1% of inflow), the onset of transition was particularly sensitive to the inlet-disturbance spectrum. Transition inception and completion were characterized by sporadic formation and breakdown of Λ-shaped structures.

1.3. Scope of the Current Study

In the present study, we performed DNS of transitional boundary layers over BFS with two step heights; K-type transition was initiated through a narrow vibrating ribbon. In practical applications (the leading edge of engine nacelles, for instance) a pressure gradient (usually adverse) is present, which may change the transition mechanisms. For this reason, we also considered a freestream-velocity profile of the type encountered near the leading edge of engine nacelles, a region where laminar flow can be maintained by appropriate design. The freestream velocity induced a favorable and then adverse pressure gradient. Since our study concentrates on the secondary instability, the simulations do not extend to the fully developed turbulent-flow region.

Two primary objectives of our work were to seek understanding of the step-height effect on the transitional process, and to evaluate the influence of a variable freestream velocity. Time-dependent dynamics of transitional structures are not dealt with in the present paper, although visualization of instantaneous flow structures is presented providing insight into the flow evolution. In the following we will first present the numerical methodology in Section 2. Then we will validate the model in Section 3, prior to discussing the results given in Section 4. Concluding in Section 5 remarks will end the paper.

2. Methodology

The equations of conservation of mass and momentum for the incompressible flow of a Newtonian fluid are:

$$\frac{\partial u_i}{\partial x_i} = 0 \tag{1}$$

$$\frac{\partial u_i}{\partial t} + \frac{\partial}{\partial x_k}(u_k u_i) = -\frac{1}{\rho}\frac{\partial p}{\partial x_i} + \nu \nabla^2 u_i. \tag{2}$$

The indices i, j and k represent the streamwise, wall-normal and spanwise direction, respectively (also denoted by x, y and z); the corresponding velocity components are u, v, and w. ρ and ν denote fluid density and kinematic viscosity. p is the hydrodynamic pressure.

The governing Equations (1) and (2) are solved using NEK5000 [34,35]. This open-source code is based upon the spectral element method (SEM) and is high-order in spatial accuracy. It can model a wide range of problems, such as transitional and turbulent flows, low-Mach-number compressible flows, passive scalar transport, etc. Spatial discretization of velocity and pressure is implemented using a $P_N - P_{N-2}$ formulation. Here, P_N is the basis function for the velocity, i.e., Nth-order Lagrange interpolation polynomials on the Gauss–Lobatto–Legendre quadrature points. P_{N-2} is the basis function for the pressure, namely $(N-2)$th-order Lagrange interpolation polynomials on the Gauss-Legendre quadrature points (details regarding SEM can be found in [36]). The temporal discretization uses a semi-implicit scheme in which the non-linear terms are treated explicitly and the

linear ones implicitly. The implicit scheme is implemented using a backward-difference-formulation with 2nd-order accuracy and Richardson extrapolation is applied as the explicit scheme with the same order of accuracy (details regarding the temporal discretization scheme are provided in [37]).

2.1. Flow Configuration

To investigate the effect of a BFS on the secondary instability, we performed DNSs of the spatially developing boundary layer over a flat plate ($h/\delta_o^* = 0.0$) and BFSs with two step heights, $h/\delta_o^* = 0.5$ and 1.0. A vibrating ribbon at the wall serves to introduce perturbations by periodic blowing and suction; this approach was chosen for its efficiency in generating relatively uncontaminated T-S waves [38]. Figure 1 shows a sketch of the computational setup. δ_o^* was the displacement thickness measured at $Re_{\delta_o^*} = U_\infty \delta_o^* / \nu = 1000$ over a flat plate, and served as the reference length. The specifications of the computational domains are given in Table 1; each of the investigations employed approximately 200 million grid points. In the streamwise direction the domains in all cases extend beyond the nonlinear-breakdown, but do not reach the location where fully developed turbulence is achieved. In the wall-normal direction the domain height is at least $7.5\delta_{99}$ at the end of each domain. Periodic boundary conditions are used in z, and the spanwise width is determined by the wavelength of the 3D perturbation initially imposed. We used a wavenumber $k_z = 0.22$, so that $-\pi/k_z \leq z/\delta_o^* \leq \pi/k_z$; this is equivalent to $4.3\delta_{99}$ for $h/\delta_o^* = 0.0$ and 0.5, and $3.0\delta_{99}$ for $h/\delta_o^* = 1.0$ at the outlet, respectively. Two more calculations with BFSs were performed in which the domain was halved in the spanwise direction, i.e., $0 \leq z/\delta_o^* \leq \pi/k_z$, and a symmetric condition was used in z. The effect of a realistic freestream-velocity distribution $U_e(x)$ (details given in Section 2.2) on the instability was also investigated in a case with $h/\delta_o^* = 0.5$. A symmetry boundary condition was used in this case. In the following sections, results of ZPG cases are discussed using full domains with periodic boundary conditions unless otherwise stated.

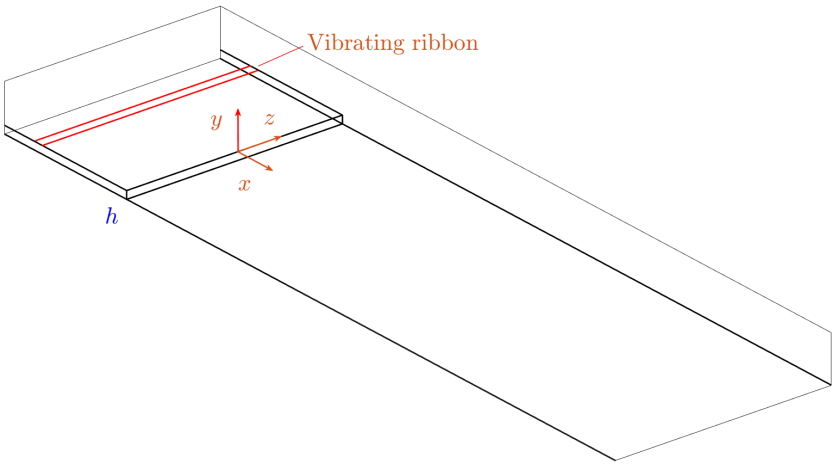

Figure 1. Sketch of the geometry used for the calculations of the boundary layer over a backward-facing step.

2.2. Boundary Conditions

No-slip conditions are applied at the walls. The velocity profile is prescribed at the inflow for the ZPG cases; the inlet Reynolds number based on local displacement thickness is $Re_{\delta^*} = 920$, so that (in the flat-plate case) $Re_{\delta^*} = 1000$ at the reference location, $x = 0$. In the ZPG cases a Blasius profile was used, whereas in the case with a variable freestream velocity we used a velocity distribution of the type encountered on engine nacelles. Many studies[14,20,21,39,40] considered surface imperfections located between 10–30% of the chord; we followed the same approach: the velocity at the inflow was taken from the location at 16% of the chord, the imperfection was at 20% of the chord, and the outlet was at 31% of the chord.

Table 1. Numerical setup for the boundary layers over backward-facing steps. (S) denotes cases in which symmetry boundary conditions were applied at $z = 0$.

Case	h/δ_o^*	h/δ_{99}	$L_x/\delta_o^* \times L_y/\delta_o^* \times L_z/\delta_o^*$	$N_x \times N_y \times N_z$
Flat plate	0.0	0.0	$350 \times 75 \times 2\pi/k$	$1184 \times 449 \times 337$
Small step	0.5	0.175	$250 \times 75 \times 2\pi/k$	$1254 \times 470 \times 337$
Large step	1.0	0.350	$250 \times 75 \times 2\pi/k$	$1254 \times 491 \times 337$
Variable U_e (S)	0.5	0.175	$200 \times 40 \times \pi/k$	$1590 \times 393 \times 169$
Small step (S)	0.5	0.175	$250 \times 75 \times \pi/k$	$1254 \times 470 \times 169$
Large step (S)	1.0	0.350	$250 \times 75 \times \pi/k$	$1254 \times 491 \times 169$

A convective boundary condition is applied at the outflow:

$$[-p\boldsymbol{I} + \nu(\nabla \boldsymbol{u})] \cdot \boldsymbol{n} \;=\; 0. \tag{3}$$

Here $\boldsymbol{I}$ is the identity matrix, $\boldsymbol{u}$ the velocity vector and $\boldsymbol{n}$ the unit normal to the boundary. The farfield boundary also uses (3), except that it enforces a given freestream-velocity distribution, U_e/U_∞. For the ZPG case, the freestream velocity was equal to U_∞. The variable distribution of U_e/U_∞ was provided by Bombardier Aerospace (Personal communication), and corresponds to that encountered on an engine nacelle. The wall-normal edge velocity, V_e, was obtained from conservation of mass, and the pressure along the freestream boundary was obtained from the Bernoulli equation (details given in Ref. [41]). As mentioned before, we only consider the region between 16% and 31% of the nacelle chord-length. The freestream profile of velocity and the dimensionless pressure parameter

$$K = \frac{\nu}{U_e^2}\frac{dU_e}{dx} \tag{4}$$

are shown in Figure 2.

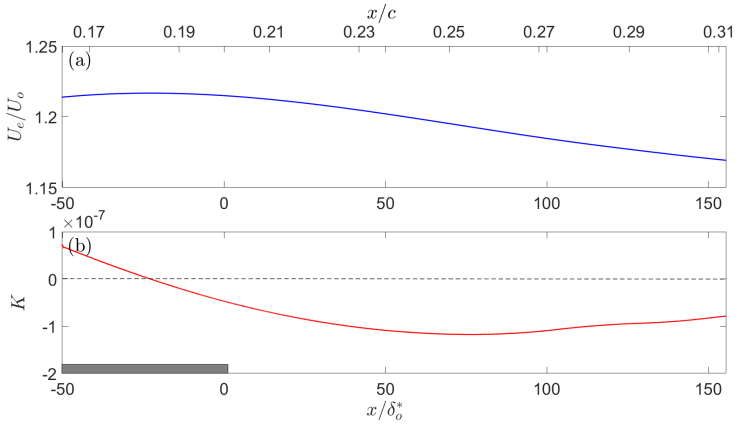

Figure 2. Freestream profiles of (**a**) velocity, U_e/U_∞ and (**b**) pressure gradient, K; the top axis is in chord length unit, x/c. The grey area shows the position of the step.

A spanwise extent of one wavelength with periodic boundary conditions is used for the full domain. In the half-domain cases a symmetric condition is imposed in the spanwise direction at $z = 0$. The use of symmetric conditions is justified to the non-linear stages of the transition. Figure 3 compares the profiles of the skin-friction coefficient

$$C_f = \frac{2\tau_w}{\rho U_\infty^2}, \tag{5}$$

where τ_w is the wall shear stress. The agreement between full and half domains remains good beyond the over-shoot; discrepancy then becomes non-negligible as C_f evolves further

downstream. Close to the peak of C_f, a maximum discrepancy of 5.0% is observed. The coherent structures are not really affected (Figure 4), and the local values of the second moments differ, on average, by less than 2%, with only a small, very localized, peak of the order of 15% occurring at centerline (not shown).

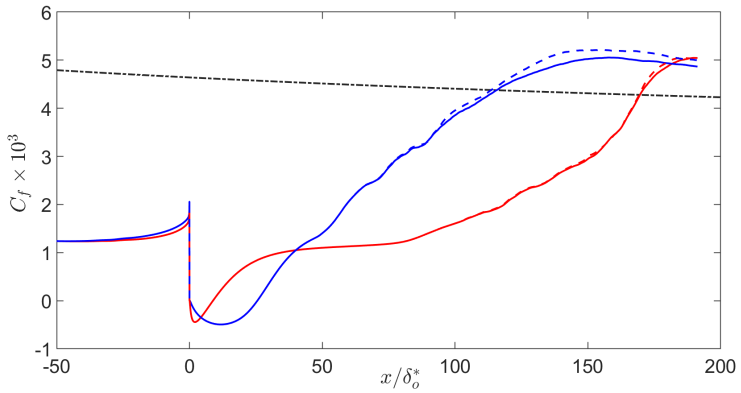

Figure 3. Skin−friction coefficient, C_f: Full domain *vs.* Half domain. ——, – – – Small step; ——, – – – large step. The solid line denotes the full domain, the dashed line the corresponding half domain. —·— Turbulent correlation [42].

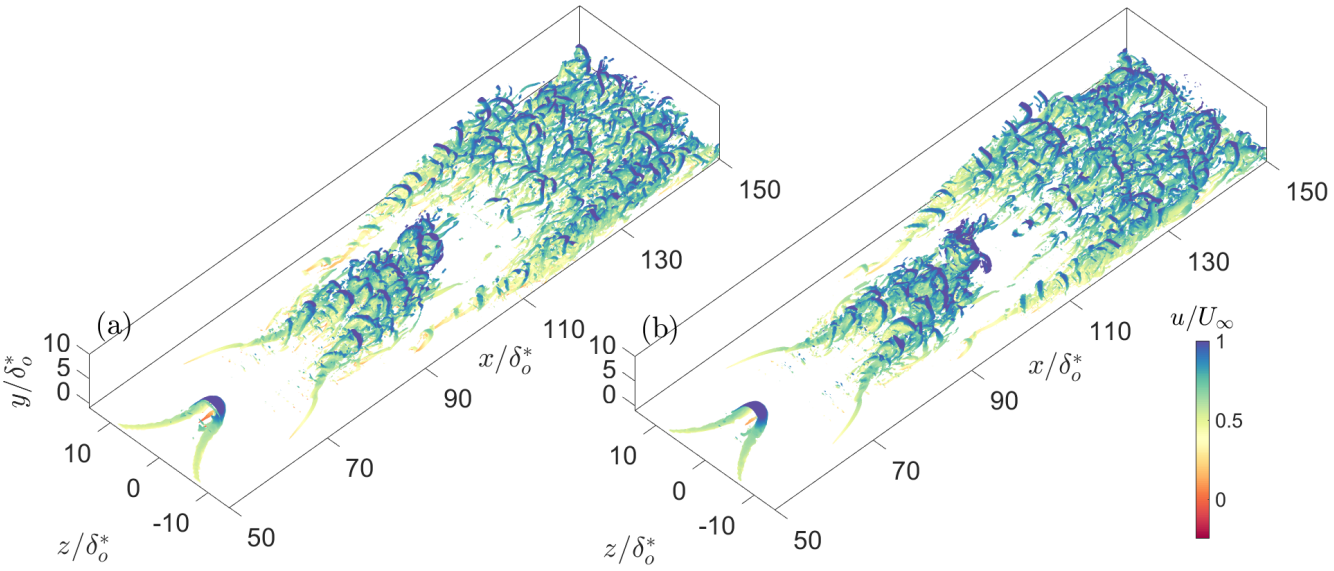

Figure 4. Large step. Isosurfaces of λ_2, colored by the magnitude of streamwise velocity, u/U_∞; $\lambda_2 = -3.0 \times 10^{-2}$. (**a**) Full domain; (**b**) half domain.

The wall-normal velocity over the simulated vibrating ribbon is prescribed as follows [43]:

$$v(x,z,t) = A_1 f(x)\sin(\omega_x t) + A_2 f(x) g(z)\sin(\omega_z t), \tag{6}$$

where $A_1/U_\infty = 0.2\%$ and $A_2/U_\infty = 0.05\%$ are the amplitudes of the fundamental and oblique waves. ω_x and ω_z are their frequencies; for K-type transition, $\omega_x = \omega_z$. The non-dimensional frequency is $F = \omega_x \nu/U_\infty^2 \times 10^6 = 100$. $g(z) = \cos(2\pi z/\lambda_z)$ is a spanwise modulation function and $\lambda_z = 2\pi/k_z$. $f(x)$ is defined as:

$$f(x) = 15.1875\xi^5 - 35.4375\xi^4 + 20.25\xi^3; \tag{7}$$

where ξ is given by:

$$\xi = \frac{x - x_{R1}}{x_c - x_{R1}} \text{ for } x_{R1} < x < x_c, \text{ and} \tag{8}$$

$$\xi = \frac{x_{R2} - x}{x_{R2} - x_c} \text{ for } x_c < x < x_{R2}. \tag{9}$$

$x_c = (x_{R1} + x_{R2})/2$ is the center of vibrating ribbon, which extends from $x_{R1} = -40\delta_o^*$ to $x_{R2} = -20\delta_o^*$. For the frequency imposed the reference location corresponds to the most unstable region in the neutral stability curve for a ZPG boundary layer.

3. Model Validation

NEK5000 has been extensively used for the simulation of transitional flows [41,44–46]; we further validated the model by considering the evolution of small perturbations in a 2D boundary layer, by testing the freestream boundary condition to verify that the favorable and adverse pressure-gradients were implemented correctly, and by performing a grid-convergence study.

A Blasius boundary layer was first simulated with $Re_\delta^* = 400$ at the inlet and $Re_\delta^* = 1225$ at the outlet; 7th-order polynomials were used. Figure 5 shows the amplification of the perturbation, quantified using the integral in the wall-normal direction of twice the perturbation kinetic energy (PKE) $\mathcal{K}$, i.e.,

$$\mathcal{A} = \int_0^\infty 2\mathcal{K} dy = \int_0^\infty (\overline{u'^2} + \overline{v'^2})\, \mathrm{d}y, \tag{10}$$

where overbar denotes the time average over one period of the vibrating ribbon. We considered a frequency $F = 140 \times 10^{-6}$ for the instability waves with an initial amplitude $A_1 = 1 \times 10^{-4} U_\infty$, to compare with Case 1 in Ref. [43]. Good agreement with the reference data is achieved and the locations of Branch I and Branch II are consistent with the results in the literature [26,47–49]. The perturbation amplitude profiles (not shown here) were also in very good agreement with those in the literature.

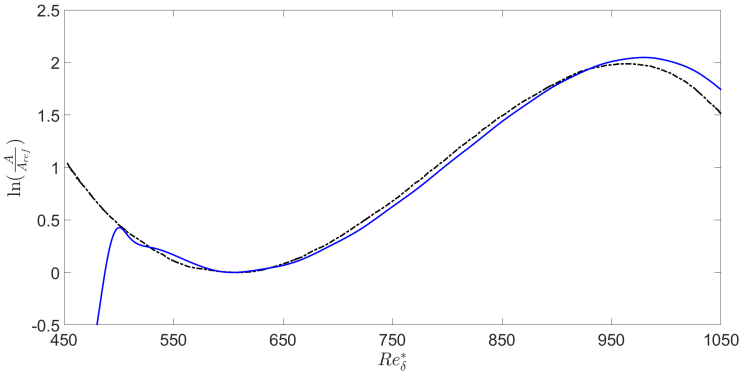

Figure 5. Amplification curves; $\mathcal{A}_{ref}$ is evaluated at the Branch I location, $Re_{\delta^*} = 605$. —— 2D DNS; —·— Fasel & Konzelmann [43].

We then validated the implementation of the freestream boundary condition by performing the simulation of a laminar Falkner–Skan flow. At the inflow, $Re_\delta^* = 800$ and the exact velocity profile was prescribed. $U_\infty(x)$ at the freestream is given by:

$$U_\infty(x) = \left(1 + \frac{x}{x_o}\right)^m, \tag{11}$$

where x_o is the distance between the leading edge of the flat plate and the inlet of the domain, and $m = -0.065$ was used (corresponding to $\beta_H = -0.14$). The base flow was in excellent agreement with the exact solution, and, when a perturbation with frequency

$F = 140 \times 10^{-6}$ and amplitude $A = 1 \times 10^{-7} U_o$ (U_o denotes the freestream velocity at inflow) was introduced, the predicted Branch II location agreed well with the data from the spatial stability analysis [26,50]; the discrepancy was around 9%.

The grid was refined near the step by decreasing the size of each spectral element by 5% upstream of the step, and then increasing it again by 5% downstream of the step. The elements were also stretched by 5% in y, and constant in z. Near the step, $\Delta x_{min}/\delta_o^* \times \Delta y_{min}/\delta_o^* \times \Delta z/\delta_o^* = 0.0130 \times 0.0106 \times 0.080$. A grid-convergence study was performed for the large-step case by comparing 5th- and 7th-order polynomials. A comparison of two polynomial-order results is shown in Figure 6; C_f was averaged over eight perturbation periods. Very minor discrepancies between two profiles are observed, indicating that 7th-order polynomials are appropriate for the present study.

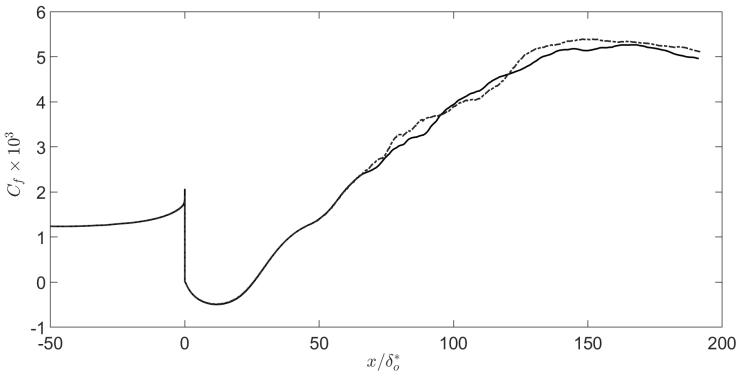

Figure 6. Skin−friction coefficient, C_f, for the large-step case. ——— 7th−order polynomials; —·— 5th−order polynomials.

4. Results

4.1. Evolution of Skin-Friction

Figure 7 presents the evolution of C_f. The BFS causes early onset of transition, compared with the flat-plate case, and the APG caused by the variable freestream velocity further increases the instability of the flow. In the step cases, Figure 7a, non-linear effects start appearing within the recirculation region, where the amplitude of the perturbation begins to exceed 1% of U_∞. For the small step, the disturbance growth is not large enough to modify the size of the recirculation region, and, overall, the C_f profile evolves similarly to that of flat plate. The large step destabilizes the flow the most. Not only it reduces the size of the recirculation region but also modifies the overall behavior of C_f, which no longer resembles that of the flat-plate case. This change reflects the extensive role played by K-H instability mechanisms at the initial stages of transition. Regardless of the step size, the flow remains convectively unstable. In the recirculation regions the peak reverse-flow is less than 4% of local U_∞, too weak to cause local absolute instability [51–53]. Figure 7b compares the variable-U_e case with the corresponding ZPG case. The APG after the step further advances the inception of transition and increases the profile slope of C_f. The recirculation region is slightly longer, but the peak reverse velocities are similar, close to 2.0% of the local U_e.

4.2. Mean Velocity and Perturbation Amplitude

Figure 8 shows the mean velocity and the *rms* profiles of u' at selected locations. In the recirculation region, Figure 8a, the mean-velocity profiles collapse above the local inflection point in the ZPG cases; the separated-flow zone only displaces the flow upward, but does not change the velocity profile. The case with variable U_e has a fuller velocity profile, reflecting the FPG upstream of the step. More significant differences can be observed in the reattachment zone and beyond, Figure 8b. The small-step case returns towards a Blasius-like profile earlier than the large-step case, and the variable-U_e case maintains its FPG-like shape. Further downstream, Figure 8c, the mean-velocity profiles begin to diverge,

as the large-step case moves towards a turbulent-like profile faster than the other cases; the velocity profile matches the standard equilibrium logarithmic-law slightly beyond the peak of the over-shoot, i.e., at $x/\delta_o^* = 170$, although the C_f is still 5.5% higher than the turbulent correlation. In the small-step cases the mean-velocity profiles approach, but never reach, a logarithmic behavior.

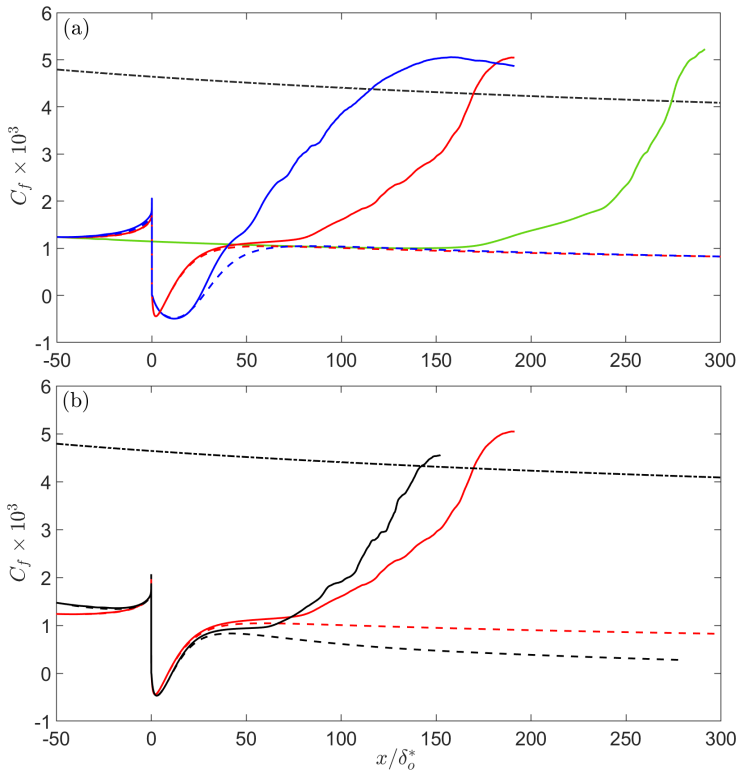

Figure 7. Skin−friction coefficient, C_f. (**a**) Step-height effect; (**b**) influence of variable U_e. —— Flat plate; ——, – – – small step; ——, – – – large step; ——, – – – small step, variable U_e. The solid line is the transitional flow, the dashed line the corresponding laminar flow. —·— Turbulent correlation [42].

The u'_{rms} profiles initially present a typical two-peak structure characteristic of T-S waves, Figure 8d; in the recirculation region, however, a third peak (Peak ③) appears immediately downstream of the steps, in correspondence of the inflection point observed in Figure 8a; the destabilization mechanism switches from viscous instability to a combination of viscous and K-H instability. Peak ③ increases in amplitude as the perturbation propagates downstream and eventually exceeds Peak ②, Figures 8e,f, indicating that the viscous instability is becoming predominant. Non-linear effects are generally considered negligible if $u'_{\text{rms}} < 0.01U_e$. This occurs well within the recirculation region, compared with a flat-plate case in which it would not occur until $x/\delta_o^* = 58$. Additionally, note how the APG causes the intermediate peak ② to grow faster than in the ZPG small-step case, so that the u'_{rms} levels are comparable to those of the more unstable large-step case. The intermediate peak persists longer in the large-step case, Figure 8e, as a consequence of the longer recirculation region and its associated shear-layer instability. Further downstream, Figure 8f, the profiles tend towards the standard turbulent shape and magnitude (in outer units), since the wall stress is significantly lower than the turbulent one; however, the peak u'_{rms} is much higher than the turbulent one in wall units.

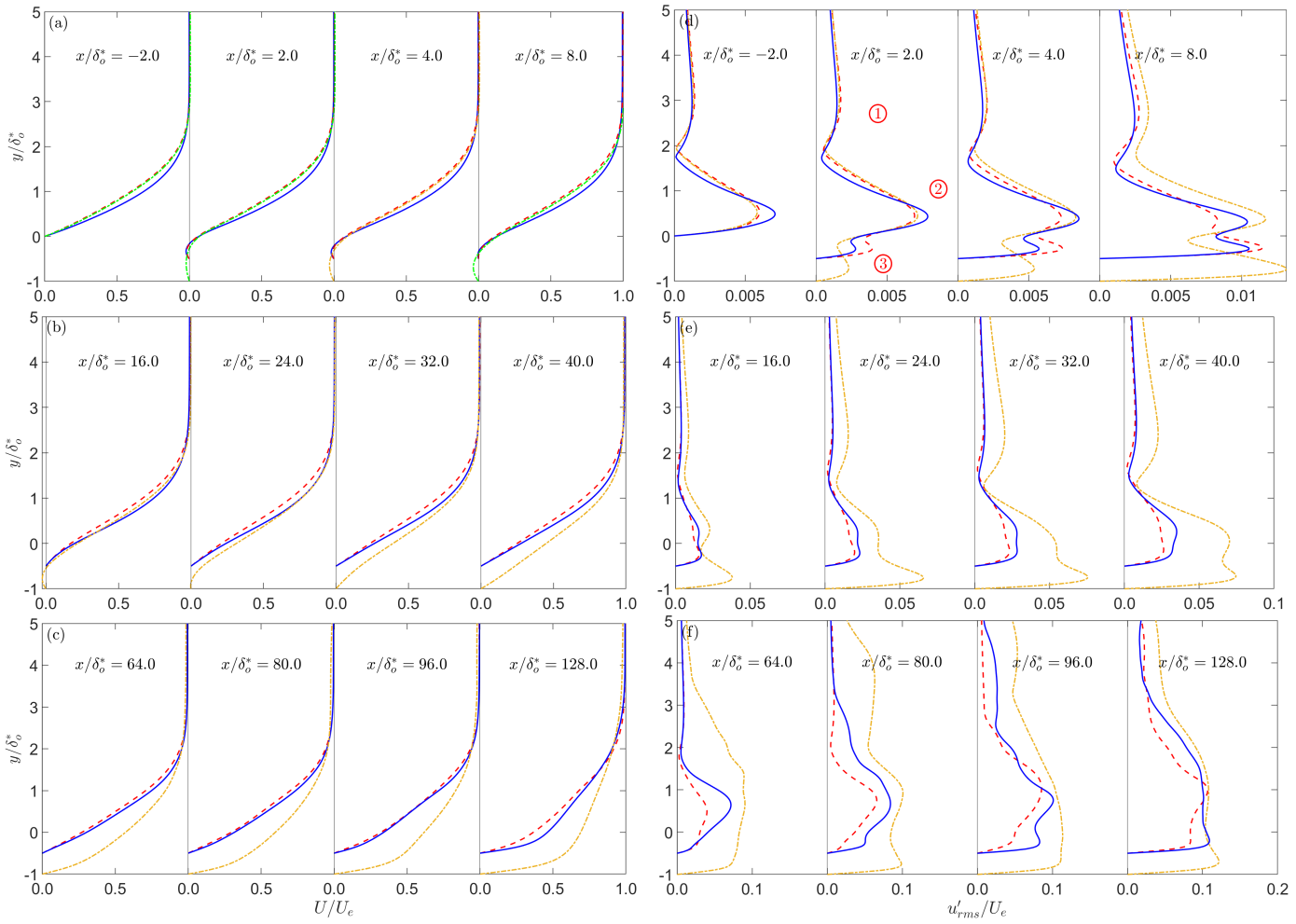

Figure 8. Profiles of (**a**–**c**) mean velocity and (**d**–**f**) u'_{rms} at selected locations. – – – Small step; ——— small step, variable U_e; – – – , – – – large step.

Figure 9 shows contours of u'_{rms}. Peak ② propagates along the inflection point, $\partial^2 U/\partial y^2 = 0$ while peak ③ moves away from the wall, and eventually merges with peak ②. The growth of the perturbation along the inflection point reflects the important role played by the K-H instability mechanism in the transition process. In the small-step case, the combined effect of separation and APG yields a more unstable flow in the variable-U_e case. This behavior is typical of transition in a separation bubble; the perturbation grows in the outer region of the recirculation where the separated shear-layer is unstable via the inviscid K-H instability, while in the inner region the reversed flow near the wall is susceptible to the viscous instability [11,54].

4.3. Instantaneous Flow Structures

Figures 10–12 show the instantaneous vortical structures inside the boundary layer. The iso-surfaces are visualized using the λ_2 criterion [55] (λ_2 is the middle eigenvalue of the strain-rate tensor), colored by the magnitude of the streamwise velocity (u/U_e for the variable U_e case); various values of λ_2 are used to highlight the flow features in different regions. In the large-step case (Figure 10) a large-scale Λ-shaped vortical structure spans the domain. This structure evolves from the spanwise vortices formed immediately downstream of the step as a result of the K-H instability of the separated shear-layer [23], Figure 10b. These vortices form kinks that stretch and lift up due to self-induction, eventually resulting in hairpin-shaped structures, Figure 10c. Shortly after the hairpin head is lifted up small-scale structures start to form, eventually leading to a turbulent-like, random distribution of hairpins. In the small-step case, the vortical structures evolve

similarly to those in the large-step one near the step, Figure 11b. The smaller recirculation region, however, limits the development of the 2D rollers; the formation and breakdown of the hairpin vortices are, therefore, delayed. Although the small step accelerates the onset of transition, the overall evolution of the flow structures resembles that of a conventional flat plate, Figure 11a; the characteristic aligned pattern of Λ-shaped vortices, typical of K-type transition, is clear. The variable U_e further accelerates the transition process, Figure 12, without modifying the coherent structures.

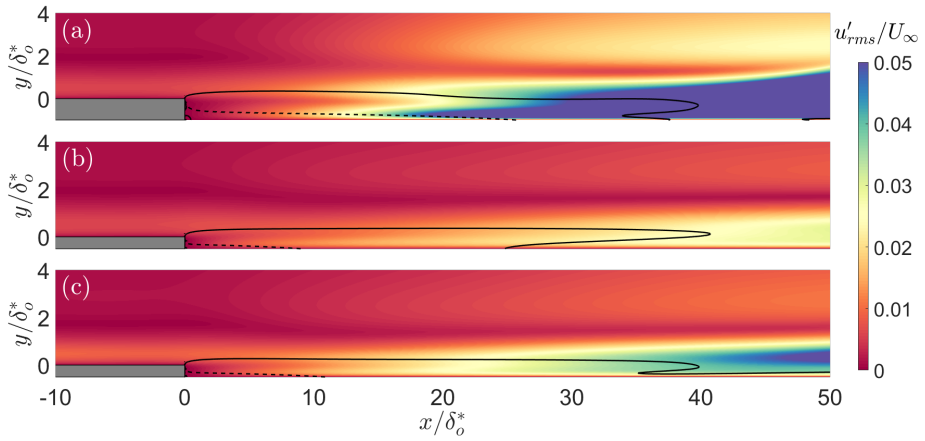

Figure 9. Contours of u'_{rms}. (**a**) Large step; (**b**) small step; (**c**) small step, variable U_e. —— $\partial^2 U/\partial y^2 = 0$; − − − $\partial U/\partial y = 0$. Different scales are used on x and y axes.

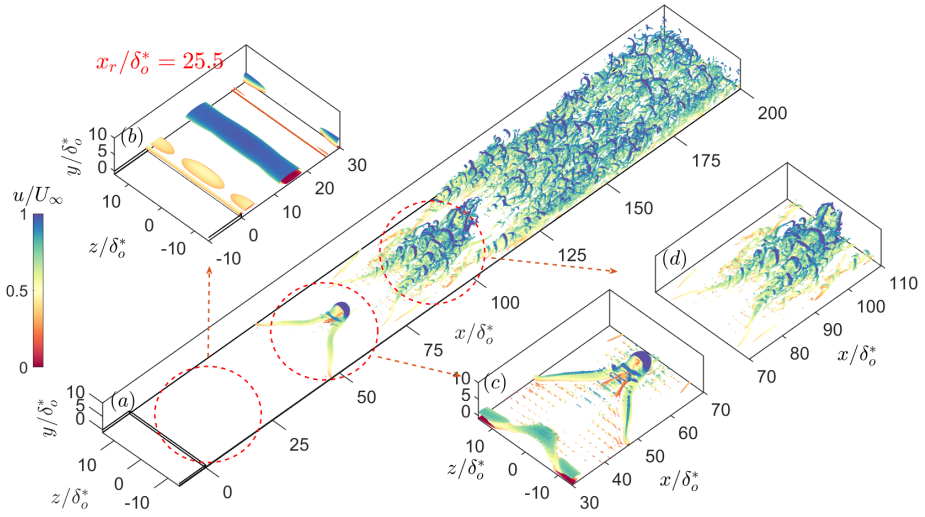

Figure 10. Large step. Isosurfaces of λ_2, colored by the magnitude of streamwise velocity, u/U_∞. (**a**) $\lambda_2 = -2.0 \times 10^{-2}$; (**b**) $\lambda_2 = -2.5 \times 10^{-4}$; (**c**) $\lambda_2 = -2.5 \times 10^{-3}$; (**d**) $\lambda_2 = -2.5 \times 10^{-2}$.

Figures 13–15 show contours of the instantaneous streamwise velocity, u/U_∞, in the $xz-$plane at $y/\delta_o^* = 1.0$ for the ZPG cases. Please note that the flat-plate case has been shifted so that the location where the domain ends is the same for all cases. Two instants separated by one period of the vibrating ribbon, T, are shown. The flat-plate case (Figure 13) exhibits both periodicity in time and symmetry throughout the domain. The small-step case (Figure 14), on the other hand, begins to lose periodicity by $x/\delta_o^* = 150$ (corresponding to $x/\delta_o^* = 250$ in the flat-plate case); the flow field remains symmetric to the end of the domain. In the large-step case (Figure 15) the shear-layer instability discussed before causes the non-linear effects to become significant much earlier, and the flow loses both periodicity and symmetry by $x/\delta_o^* = 95$.

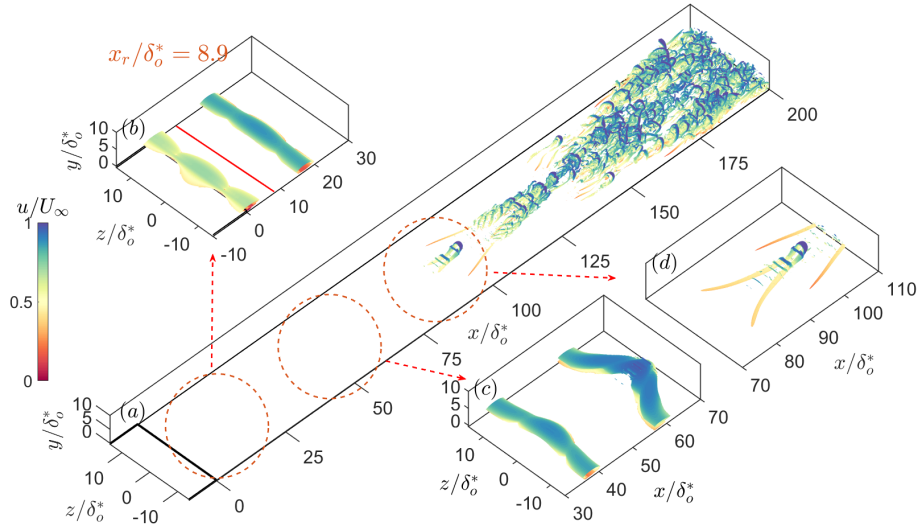

Figure 11. Small step. Isosurfaces of λ_2, colored by the magnitude of streamwise velocity, u/U_∞. (**a**) $\lambda_2 = -2.0 \times 10^{-2}$; (**b**) $\lambda_2 = -2.5 \times 10^{-4}$; (**c**) $\lambda_2 = -5.0 \times 10^{-4}$; (**d**) $\lambda_2 = -1.0 \times 10^{-2}$.

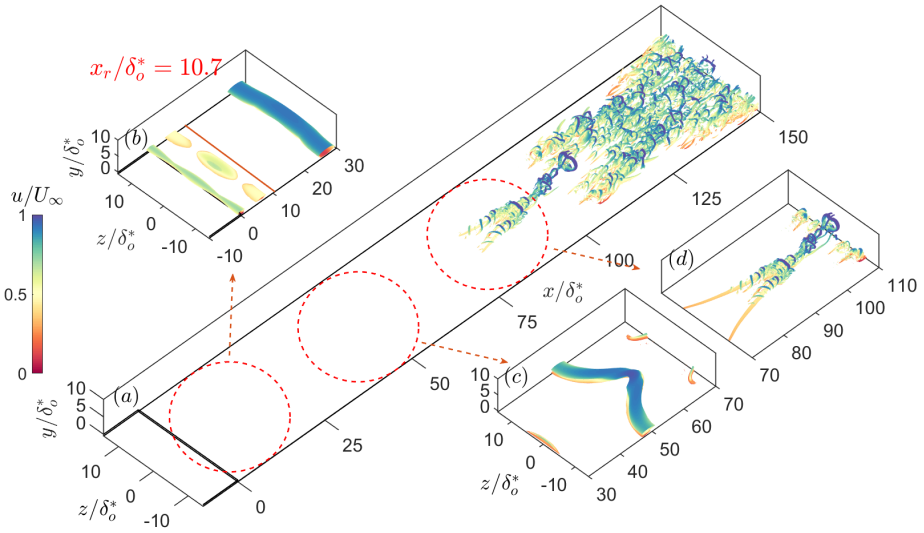

Figure 12. Small step, variable U_e. Isosurfaces of λ_2, colored by the magnitude of streamwise velocity, u/U_e. (**a**) $\lambda_2 = -2.0 \times 10^{-2}$; (**b**) $\lambda_2 = -1.5 \times 10^{-4}$; (**c**) $\lambda_2 = -3.0 \times 10^{-4}$; (**d**) $\lambda_2 = -1.0 \times 10^{-2}$.

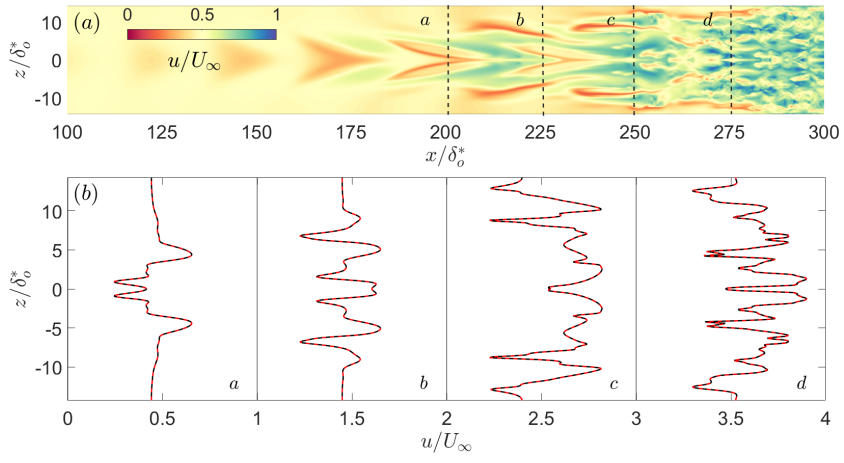

Figure 13. Flat plate. Instantaneous streamwise velocity in the $y_{wall}/\delta_o^* = 1.0$ plane. (**a**) Velocity contours; (**b**) velocity profiles at the locations indicated by dashed lines in (**a**). —— $t = t_o$; – – – $t = t_o + T$.

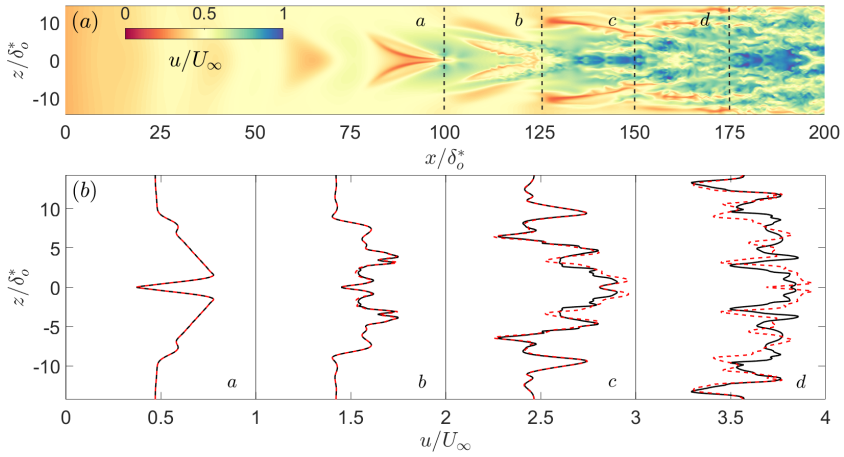

Figure 14. Small step. Instantaneous streamwise velocity in the $y_{wall}/\delta_o^* = 1.0$ plane. (**a**) Velocity contours; (**b**) velocity profiles at the locations indicated by dashed lines in (**a**). ——— $t = t_o$; – – – $t = t_o + T$.

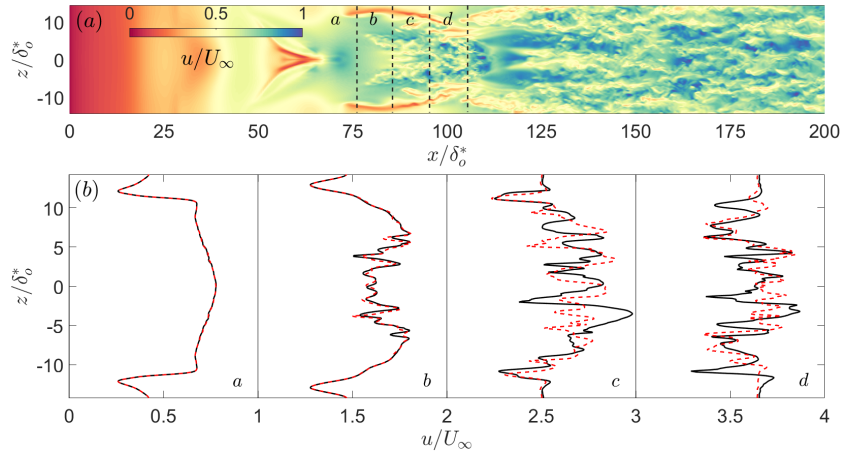

Figure 15. Large step. Instantaneous streamwise velocity in the $y_{wall}/\delta_o^* = 1.0$ plane. (**a**) Velocity contours; (**b**) velocity profiles at the locations indicated by dashed lines in (**a**). ——— $t = t_o$; – – – $t = t_o + T$.

4.4. Perturbation Kinetic-Energy Budgets

The transport equation of the perturbation kinetic energy (PKE), $\mathcal{K} = \langle u_i' u_i' \rangle / 2$ (angle brackets denote averaging over time and the spanwise direction) is given by [56]:

$$\frac{\partial \mathcal{K}}{\partial t} + \underbrace{\frac{\partial}{\partial x_k}(\langle U_k \rangle \mathcal{K})}_{C} = \underbrace{-\langle u_i' u_k' \rangle \frac{\partial \langle U_i \rangle}{\partial x_k}}_{P} \underbrace{-\frac{1}{2}\frac{\partial}{\partial x_k}\langle u_i' u_k' \rangle}_{T} \underbrace{-\frac{1}{\rho}\frac{\partial}{\partial x_k}\langle p' u_k' \rangle}_{\Pi^t} \underbrace{-\nu \left\langle \frac{\partial u_i'}{\partial x_k}\frac{\partial u_i'}{\partial x_k} \right\rangle}_{\varepsilon} + \underbrace{\nu \nabla^2 \mathcal{K}}_{D}, \tag{12}$$

where P is the production, ε the pseudo-dissipation, D the viscous diffusion, T the turbulent transport, Π^t the pressure transport, and C the convection, respectively.

The budget terms at $x/\delta_o^* = 10$ are shown in Figure 16. At the streamwise location selected the weakly non-linear effects initially occur in the step cases; terms are scaled using ν and local U_e. Pressure transport dominates as a gain term, balancing viscous diffusion immediately above the wall; this balance extends to the edge of inner layer, $y/\delta_{99}^* = 0.1$, before pressure transport switches signs and balances production and convection. As distance further increases, pressure work and convection reach a balance, which is main-

tained beyond the edge of the boundary layer. Neither the step height, Figures 16a,c, nor the freestream pressure gradient, Figure 16b, modify the budget characteristics; only the magnitude of the various terms is increased. The production, which represents the energy transfer from the mean flow to the perturbations, always has a peak near the inflection point (the second vertical line in Figures 16a–c); this phenomenon is observed throughout the flow field, as indicated in Figure 16d which shows the region of high production always straddling the inflection point. Finally, unlike what is observed in equilibrium boundary layers, the convection here plays a significant role, transferring energy away from the wall, and pressure work balances the production through most of the boundary layer, but changes sign and becomes the predominant gain term in the outer region of the flow.

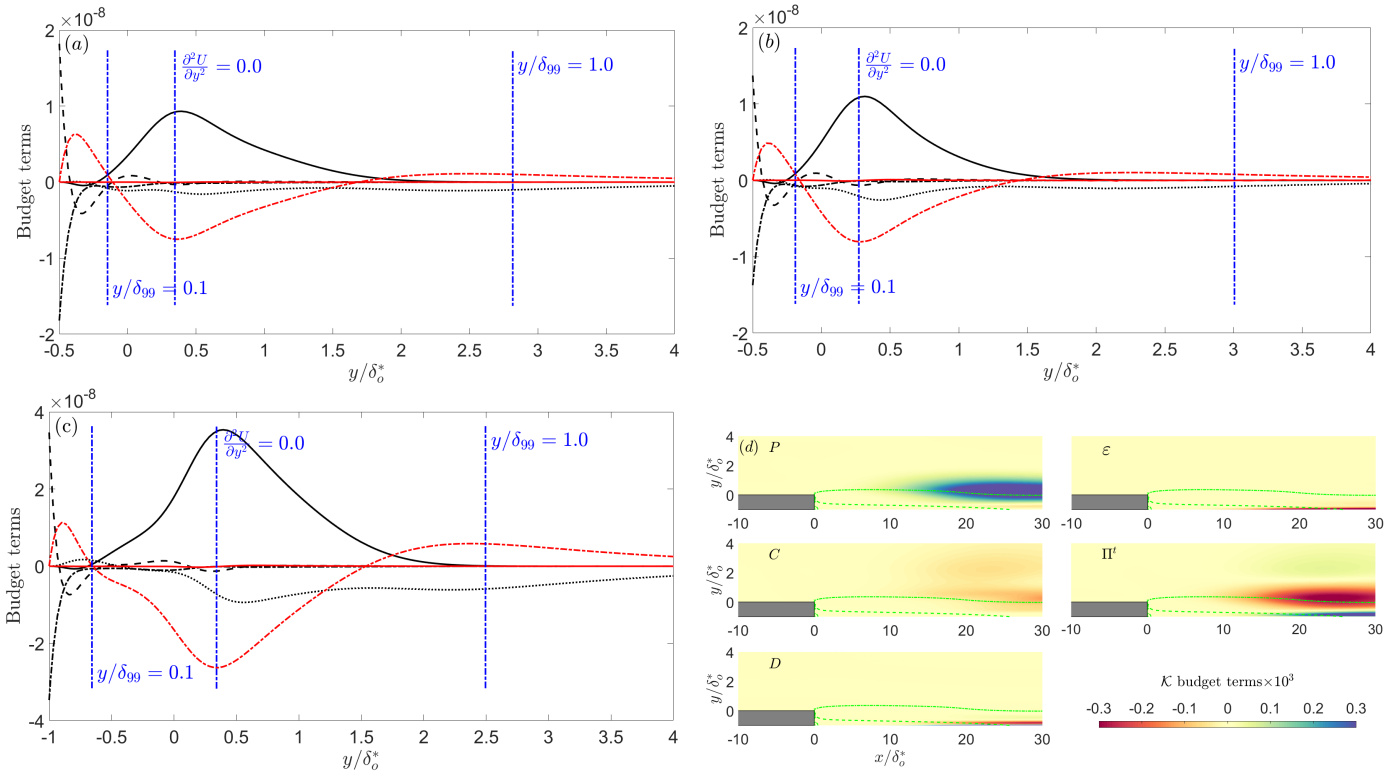

Figure 16. Budget of $\mathcal{K}$ at $x/\delta_o^* = 10$. (**a**) Small step; (**b**) small step, variable U_e; (**c**) large step; (**d**) large step; contours of $\mathcal{K}$ budget terms near the step. —— P; —·— ε; – – – D; ····· C; —— T; —·— Π^t; —·— $\partial^2 U/\partial y^2 = 0$; – – – $\partial U/\partial y = 0$.

5. Conclusions

We performed direct numerical simulations of transitional boundary layers over a backward-facing step with two step heights. We also considered a freestream-velocity profile of the type encountered on the engine-nacelle lip; this induced a favorable and then adverse pressure gradient in the domain. Our investigation sought to explore the effect of the backward-facing step sizes and evaluate the influence of an induced pressure-gradient on the secondary instability and, therefore, the domain only extended to the non-linear breakdown region. A controlled K-type transition was induced using a narrow ribbon upstream of the step that introduced small and monochromatic perturbations by periodic blowing and suction.

First, we found that the step height and the variable freestream velocity influenced the transition to turbulence significantly. In the large-step case, in particular, rapid transition occurred primarily due to the Kelvin–Helmholtz instability downstream of step. The non-linear interactions initially occurred within the recirculation region, and large-scale Λ-shaped vortical structure were formed. Second, we observed that the initial symmetry and periodicity of the flow broke down by the middle stage of transition where the slope of the skin-friction profile increased. The step height and freestream-velocity distribution affected

the location where this occurred. In contrast, we observed that in the small-step case transition occurs far downstream of the step, and the flow remained spatially symmetric and temporally periodic until the late stages of transition. Although the transition to turbulence was promoted significantly, the overall evolution of the flow field (i.e., skin-friction profile and coherent structures) resembled that of a flat-plate case. The effect of a variable freestream velocity also advanced the onset of transition to turbulence, but did not fundamentally modify the flow features, compared with the corresponding zero-pressure-gradient step case. From the budget analysis, effects of a backward-facing step and induced pressure-gradient both increase, rather than modify, the energy transfer from mean flow to perturbations; this primarily occurs along the inflection point near the step.

The present work was limited to the K-type transition; the step heights considered and the variable freestream velocity may introduce different physical mechanisms when the instability mechanisms are different (bypass transition or crossflow instability, for instance). These are issues that require further attention. In the future, other types of surface imperfections (forward-facing steps, cavities, undulations etc.) need to be considered, to evaluate whether they simply change the location of the onset of transition, or if they alter its mechanisms. Three-dimensional shapes (such as those produced by ice depositions) also need to be studied.

Author Contributions: Conceptualization, M.T. and U.P.; methodology, M.T. and U.P.; software, M.T.; validation, M.T. and U.P.; formal analysis, M.T.; investigation, M.T. and U.P.; resources, U.P.; data curation, M.T.; writing—original draft preparation, M.T.; writing—review and editing, U.P.; visualization, M.T.; supervision, U.P.; project administration, U.P.; funding acquisition, U.P. Instability and transition of a boundary layer over a backward-facing step. All authors have read and agreed to the published version of the manuscript.

Funding: This research was funded by Mitacs (IT09711), Bombardier Aerospace and CARIC/CRIAQ (Joint) (COMP-1602).

Data Availability Statement: Data can be obtained by request.

Acknowledgments: U.P. acknowledges the support from the Natural Science and Engineering Research Council of Canada (NSERC) under the Discovery Grant program, and the Canada Research Chair program. This research was enabled in part by computational support provided by Compute Ontario (computeontario.ca; last accessed on 13 November 2021) and Southern Ontario Smart Computing Innovation Platform (SOSCIP) (www.soscip.org; last accessed on 13 November 2021).

Conflicts of Interest: The authors declare no conflict of interest.

References

1. Kachanov, Y.S. Physical mechanisms of laminar boundary-layer transition. *Annu. Rev. Fluid Mech.* **1994**, *26*, 411–482. [CrossRef]
2. Wu, X.; Moin, P. Direct numerical simulation of turbulence in a nominally zero pressure-gradient flat-plate boundary-layer. *J. Fluid Mech.* **2009**, *630*, 5–41. [CrossRef]
3. Holmes, B.J.; Obara, C.J.; Martin, G.L.; Domack, C.S. Manufacturing tolerances for natural laminar flow airframe surfaces. *SAE Trans.* **1985**, *94*, 522–531.
4. Nayfeh, A.H.; Ragab, S.A.; Al-Maaitah, A.A. Effect of bulges on the stability of boundary layers. *Phys. Fluids* **1988**, *31*, 796–806. [CrossRef]
5. Choudhari, M.; Streett, C. Theoretical prediction of boundary-layer receptivity. In Proceedings of the AIAA Fluid Dynamics Conference, Colorado Springs, CO, USA, 20–23 June 1994; p. 2223.
6. Eppink, J.L. Mechanisms of stationary cross-flow instability growth and breakdown induced by forward-facing steps. *J. Fluid Mech.* **2020**, *897*, A15(1)–A15(30). [CrossRef]
7. Klebanoff, P.S.; Tidstrom, K.D. Mechanism by which a two-dimensional roughness element induces boundary-Layer transition. *Phys. Fluids* **1972**, *15*, 1173–1188. [CrossRef]
8. Dovgal, A.V.; Kozlov, V.V. Hydrodynamic instability and receptivity of small-scale separation regions. In *Laminar-Turbulent Transition*; Springer: Berlin/Heidelberg, Germany, 1990; pp. 523–531.
9. Dovgal, A.V.; Kozlov, V.V.; Michalke, A. Laminar boundary-layer separation: instability and associated phenomena. *Prog. Aerosp. Sci.* **1994**, *30*, 61–94. [CrossRef]
10. Roberts, S.K.; Yaras, M.I. Boundary-layer transition affected by surface roughness and free-stream turbulence. *J. Fluids Eng.* **2005**, *127*, 449–457. [CrossRef]

11. Brinkerhoff, J.R.; Yaras, M.I. Interaction of viscous and inviscid instability modes in separation-bubble transition. *Phys. Fluids* **2011**, *23*, 124102. [CrossRef]
12. Saric, W.S.; Reed, H.L.; White, E.B. Stability and transition of three-dimensional boundary-layers. *Annu. Rev. Fluid Mech.* **2003**, *35*, 413–440. [CrossRef]
13. Eppink, J.L.; Wlezien, R.W.; King, R.A.; Choudhari, M. Interaction of a backward-facing step and crossflow instabilities in boundary-layer transition. *AIAA J.* **2018**, *56*, 497–509. [CrossRef] [PubMed]
14. Eppink, J.L.; Wlezien, R.W.; King, R.A.; Choudhari, M. Influence of a backward-facing step on swept-wing boundary-layer transition. *AIAA J.* **2019**, *57*, 267–278. [CrossRef]
15. Crouch, J.D. Theoretical studies on the receptivity of boundary layers. In Proceedings of the AIAA Fluid Dynamics Conference, Colorado Springs, CO, USA, 20–23 June 1994; p. 2224.
16. Crouch, J.D.; Kosorygin, V.S.; Ng, L.L. Modeling the effects of steps on boundary-layer transition. In *IUTAM Symposium on Laminar-Turbulent Transition*; Springer: Dordrecht, Netherlands, 2006; pp. 37–44.
17. Boiko, A.V.; Dovgal, A.V.; Kozlov, V.V.; Shcherbakov, V.A. Flow instability in the laminar boundary-layer separation zone created by a small roughness element. *Fluid Dyn.* **1990**, *25*, 12–17. [CrossRef]
18. Danabasoglu, G.; Bringen, S.; Streett, C. Spatial simulation of boundary-layer instability—Effects of surface roughness. In Proceedings of the AIAA 31st Aerospace Sciences Meeting, Reno, NV, USA, 11–14 January 1993. ; p. 75.
19. Wang, Y. Instability and Transition of Boundary-Layer Flows Disturbed by Steps and Bumps. Ph.D. Thesis, Queen Mary University of London, London, UK, 2004.
20. Wang, Y.X.; Gaster, M. Effect of surface steps on boundary-layer transition. *Exp. Fluids* **2005**, *39*, 679–686. [CrossRef]
21. Duncan Jr, G.T. The Effects of Step Excrescences on Swept-Wing Boundary-Layer Transition. Ph.D. Thesis, Texas A&M University, College Station, TX, USA, 2014.
22. Eppink, J.L. Effect of step shape on transition over a swept backward-facing step. In *AIAA Aviation 2020 Forum*; American Institute of Aeronautics and Astronautics: Reston, VA, USA, 2020; p. 3051.
23. Hu, W.; Hickel, S.; Van Oudheusden, B. Dynamics of a supersonic transitional flow over a backward-facing step. *Phys. Rev. Fluids* **2019**, *4*, 103904. [CrossRef]
24. Hu, W.; Hickel, S.; Van Oudheusden, B. Influence of upstream disturbances on the primary and secondary instabilities in a supersonic separated flow over a backward-facing step. *Phys. Fluids* **2020**, *32*, 056102.
25. Schubauer, G.B.; Skramstad, H.K. *Laminar Boundary-Layer Oscillations and Transition on a Flat Plate*; Technical Report; NACA: Boston, MA, USA, 1948.
26. Wazzan, A.R.; Okamura, T.T.; Smith, A.M. *Spatial and Temporal Stability Charts for the Falkner-Skan Boundary-Layer Profiles*; Technical Report; McDonnell Douglas Astronautics CO-HB: Huntington Beach CA, USA, 1968.
27. Taghavi, H.; Wazzan, A.R. Spatial stability of some Falkner—Skan profiles with reversed flow. *Phys. Fluids* **1974**, *17*, 2181–2183. [CrossRef]
28. Gostelow, J.P.; Blunden, A.R. Investigations of boundary-layer transition in an adverse pressure-gradient. *J. Turbomach.* **1989**, *111*, 366–374. [CrossRef]
29. Walker, G.J.; Gostelow, J.P. Effects of adverse pressure-gradients on the nature and length of boundary-layer transition. *J. Turbomach.* **1990**, *112*, 196–205. [CrossRef]
30. Kloker, M.; Fasel, H.F. Numerical simulation of two-and three-dimensional instability waves in two-dimensional boundary-layers with streamwise pressure-gradient. In *Laminar-Turbulent Transition*; Springer: Berlin/Heidelberg, Germany, 1990; pp. 681–686.
31. Mislevy, S.P.; Wang, T. The effects of adverse pressure-gradients on momentum and thermal structures in transitional boundary-layers: part 1—Mean quantities. *J. Turbomach.* **1996**, *118*, 717–727. [CrossRef]
32. Borodulin, V.I.; Kachanov, Y.S.; Roschektayev, A.P. Turbulence production in an APG-boundary-layer transition induced by randomized perturbations. *J. Turbul.* **2006**, N8. [CrossRef]
33. Bose, R.; Zaki, T.A.; Durbin, P.A. Instability waves and transition in adverse pressure-gradient boundary-layers. *Phys. Rev. Fluids* **2018**, *3*, 053904. [CrossRef]
34. Fischer, P.F.; Lottes, J.W.; Kerkemeier, S.G. NEK5000. 2008. Available online: https://nek5000.mcs.anl.gov (accessed on 10 September 2019)
35. Fischer, P.F. An overlapping Schwarz method for spectral element solution of the incompressible Navier-Stokes equations. *J. Comput. Phys.* **1997**, *133*, 84–101. [CrossRef]
36. Deville, M.O.; Fischer, P.F.; Mund, E.H. *High-Order Methods for Incompressible Fluid Flow*; Cambridge University Press: Cambridge, UK, 2002.
37. Fischer, P.F. *Implementation Considerations for the OIFS/Characteristics Approach to Convection Problems*; Technical Report; Argonne National Laboratory: Lemont, IL, USA, 2003.
38. Fasel, H.F.; Rist, U.; Konzelmann, U. Numerical investigation of the three-dimensional development in boundary-layer transition. *AIAA J.* **1990**, *28*, 29–37. [CrossRef]
39. Forte, M.; Perraud, J.; Séraudie, A.; Beguet, S.; Casalis, L.G.G. Experimental and numerical study of the effect of gaps on laminar-turbulent transition of incompressible boundary-layers. *Procedia IUTAM* **2015**, *14*, 448–458. [CrossRef]
40. Rius-Vidales, A.F.; Kotsonis, M. Influence of a forward-facing step surface irregularity on swept wing transition. *AIAA J.* **2020**, *58*, 5243–5253. [CrossRef]

41. Brynjell-Rahkola, M.; Shahriari, N.; Schlatter, P.; Hanifi, A.; Henningson, D.S. Stability and sensitivity of a cross-flow-dominated Falkner–Skan–Cooke boundary layer with discrete surface roughness. *J. Fluid Mech.* **2017**, *826*, 830–850. [CrossRef]
42. White, F.M. *Viscous Fluid Flow*; McGraw-Hill: New York, NY, USA, 2006; Volume 3.
43. Fasel, H.F.; Konzelmann, U. Non-parallel stability of a flat-plate boundary-layer using the complete Navier-Stokes equations. *Journal of Fluid Mechanics* **1990**, *221*, 311–347. [CrossRef]
44. Appelquist, E.; Schlatter, P.; Alfredsson, P.H.; Lingwood, R.J. Transition to turbulence in the rotating-disk boundary-layer flow with stationary vortices. *J. Fluid Mech.* **2018**, *836*, 43–71. [CrossRef]
45. Shahriari, N.; Kollert, M.R.; Hanifi, A. Control of a swept-wing boundary-layer using ring-type plasma actuators. *J. Fluid Mech.* **2018**, *844*, 36–60. [CrossRef]
46. Jing, Z.; Ducoin, A. Direct numerical simulation and stability analysis of the transitional boundary-layer on a marine propeller blade. *Phys. Fluids* **2020**, *32*, 124102. [CrossRef]
47. Ross, J.A.; Barnes, F.H.; Burns, J.G.; Ross, M.A.S. The flat plate boundary layer. Part 3. Comparison of theory with experiment. *J. Fluid Mech.* **1970**, *43*, 819–832. [CrossRef]
48. Gaster, M. On the effects of boundary-layer growth on flow stability. *J. Fluid Mech.* **1974**, *66*, 465–480. [CrossRef]
49. Saric, W.S.; Nayfeh, A.H. Nonparallel stability of boundary-layer flows. *Phys. Fluids* **1975**, *18*, 945–950. [CrossRef]
50. Obremski, H.J.; Morkovin, M.V.; Landahl, M.; Wazzan, A.R.; Okamura, T.T. *A Portfolio of Stability Characteristics of Incompressible Boundary Layers*; Technical Report; Advisory Group for Aerospace Research and Development: Fairfax, Virginia, USA, 1969.
51. Hammond, D.A.; Redekopp, L.G. Local and global instability properties of separation bubbles. *Eur. J. -Mech.-B/Fluids* **1998**, *17*, 145–164. [CrossRef]
52. Alam, M.; Sandham, N.D. Direct numerical simulation of 'short' laminar separation-bubbles with turbulent reattachment. *J. Fluid Mech.* **2000**, *410*, 1–28. [CrossRef]
53. Theofilis, V. Global linear instability. *Annu. Rev. Fluid Mech.* **2011**, *43*, 319–352. [CrossRef]
54. Rist, U.; Maucher, U. Investigations of time-growing instabilities in laminar separation-bubbles. *Eur. J. -Mech.-B/Fluids* **2002**, *21*, 495–509. [CrossRef]
55. Jeong, J.; Hussain, F. On the identification of a vortex. *J. Fluid Mech.* **1995**, *285*, 69–94. [CrossRef]
56. Pope, S.B.; Pope, S.B. *Turbulent Flows*; Cambridge University Press: Cambridge, UK, 2000.